International Journal of Biological Macromolecules 369 (2026) 152700

Contents lists available at ScienceDirect

International Journal of Biological Macromolecules

journal homepage: www.elsevier.com/locate/ijbiomac

Polysaccharide-based microneedles loaded with botanical formulation for dual-pathway neuroimmune modulation in chemotherapy-induced nausea and vomiting

Lihua Tan [a,b,c,1], Yi Liu [d,1], Zhongli Jing [a,b,c], Rui Zhu [a,b,c], Xinhui An [d], Giulia Vanti [f], Anna Rita Bilia [f,*], Meng Wang [a,e,**], Xiaoliang Ren [d,*]

[a] State Key Laboratory of Chinese Medicine Modernization, Tianjin University of Traditional Chinese Medicine, Tianjin, 301617, China
[b] Institute of Traditional Chinese Medicine, Tianjin University of Traditional Chinese Medicine, Tianjin, 301617, China
[c] Haihe Laboratory of Modern Chinese Medicine, Tianjin, 301617, China
[d] School of Chinese Materia Medica, Tianjin University of Traditional Chinese Medicine, Tianjin, 301617, China
[e] Key Laboratory of Pharmacology of Traditional Chinese Medical Formulae, Tianjin University of Traditional Chinese Medicine, Tianjin, 301617, China
[f] Department of Chemistry Ugo Schiff, Via Ugo Schiff 6, University of Florence, Florence, 59015, Italy

ARTICLE INFO

Keywords:
Microneedle
Bletilla striata polysaccharide
Centrifugal spin-coating
Neuroimmune regulation
Chemotherapy-induced nausea and vomiting
Dai-Zhe-Shi-San

ABSTRACT

Chemotherapy-induced nausea and vomiting (CINV) remain a major clinical challenge arising from neuroimmune dysregulation and limited efficacy of conventional antiemetics subjected to hepatic metabolism. Herein, we designed a carrier-free microneedle system (DZS@BMNs) by integrating *Bletilla striata* polysaccharide (BSP) supramolecular matrices with the botanical formulation Dai-Zhe-Shi-San (DZS) to achieve dual-pathway neuroimmune modulation. The triple-helical structure of BSP forms stable hydrogen-bonded complexes with DZS, serving simultaneously as a structural scaffold and a functional biopolymer for controlled release. The resulting microneedles exhibit programmable geometry (720 μm length, 280 μm base diameter), high mechanical strength, and biphasic diffusion kinetics-rapid epidermal permeation within 2 h followed by sustained transdermal delivery over 48 h. The system also demonstrated excellent cytocompatibility (>90% viability), negligible hemolysis (<2%), and good formulation stability. Mechanistically, DZS@BMNs suppressed serotonergic and dopaminergic signaling while downregulating key pro-inflammatory mediators, thereby achieving bidirectional neuroimmune regulation along the gut-brain axis. In a cisplatin-induced pica model, treatment with DZS@BMNs significantly reduced kaolin intake by 38% compared with dexamethasone during the acute phase, accompanied by tissue-specific reductions in serotonin levels: 42% in the brain, 38% in the ileum, and 22% in plasma. Collectively, this study presents a biofunctional polysaccharide-based microneedle system that integrates botanical pharmacology with macromolecular material engineering, offering a minimally invasive and biocompatible strategy for the management of CINV.

1. Introduction

Chemotherapy-induced nausea and vomiting (CINV) remain a formidable challenge in oncology, significantly compromising patient quality of life and treatment adherence. Current pharmacologic management relies on oral or injectable formulations of 5-hydroxytryptamine type-3 (5-HT_3) receptor antagonists (e.g., ondansetron, granisetron), neurokinin-1 (NK_1) receptor antagonists (aprepitant), and corticosteroids (dexamethasone) [1–3]. Despite their clinical efficacy, these agents are constrained by intrinsic pharmacokinetic and formulation limitations. 5-HT_3 antagonists exhibit short plasma half-lives (4–9 h) [4], necessitating frequent redosing, while NK_1 antagonists suffer from extensive hepatic first-pass metabolism (>60% clearance), compromising oral bioavailability [5]. These challenges are further

* Corresponding authors.
** Correspondence to: M. Wang, State Key Laboratory of Chinese Medicine Modernization, Tianjin University of Traditional Chinese Medicine, Tianjin, 301617, China.
E-mail addresses: ar.bilia@unifi.it (A.R. Bilia), wangmeng@tjutcm.edu.cn (M. Wang), renxiaoliang@tjutcm.edu.cn (X. Ren).
[1] These authors contributed equally to this work and should be considered co-first authors.

https://doi.org/10.1016/j.ijbiomac.2026.152700
Received 4 November 2025; Received in revised form 21 May 2026; Accepted 23 May 2026
Available online 24 May 2026
0141-8130/© 2026 Elsevier B.V. All rights are reserved, including those for text and data mining, AI training, and similar technologies.

exacerbated by patient-specific factors: oropharyngeal dysphagia affects nearly half of elderly chemotherapy patients, impairing oral drug intake and elevating aspiration risk [6]. Moreover, chemotherapy-induced mucositis alters gastrointestinal drug absorption, reducing dissolution efficiency by 30–50% and contributing to unpredictable antiemetic responses. Although parenteral administration circumvents gastrointestinal barriers, it introduces injection-site complications, including tissue necrosis in up to 22% of cases with repeated dosing. These persistent limitations underscore the urgent need for non-invasive, patient-centric delivery platforms with enhanced biocompatibility and programmable release kinetics [7].

Dissolving microneedle (MN) patches have emerged as a transformative transdermal delivery strategy, combining the painlessness of hypodermic needles with the simplicity of transdermal patches [8]. Composed of water-soluble polymer arrays, MNs penetrate the stratum corneum to create transient microchannels, enabling direct delivery of therapeutics into the dermal microcirculation without stimulating dermal nerves [9]. Their geometry (including needle length, base diameter, and density) can be precisely tailored to achieve desired dosing and insertion mechanics, while the hydrophilic polymer matrix offers tunable mechanical strength and rapid enzymatic degradation, ensuring favorable biocompatibility and controlled drug release [10–12]. By bypassing gastrointestinal degradation and hepatic first-pass metabolism, MN systems minimize inter- and intra-individual variability in drug exposure and enhance bioavailability [13]. Furthermore, their capacity for sustained release reduces dosing frequency, a critical advantage for elderly patients or those with swallowing difficulties [14–16]. Despite these advantages, conventional dissolving MN systems face inherent limitations. The mechanical strength of biodegradable polymers commonly used in MNs, such as hyaluronic acid, often proves insufficient for effective skin penetration, particularly under high-humidity conditions, necessitating composite strategies to achieve adequate insertion efficiency [17]. Additionally, these conventional matrices typically lack intrinsic therapeutic activity, serving solely as passive delivery vehicles rather than contributing to the overall pharmacological effect [18]. Recent advances in botanical-material hybrids, such as tea-derived nano-assemblies (3 nm diameter) stabilized by hydrogen bonding and pi-pi interactions, inspire the integration of traditional herbal actives with engineered biomaterials [19]. Addressing both the mechanical and functional limitations of existing MN platforms, the development of intrinsically active-matrix materials represents a promising direction for next-generation transdermal delivery systems.

Natural polysaccharides have gained increasing attention as biomacromolecular materials owing to their inherent biocompatibility, biodegradability, and versatile capacity for supramolecular assembly [20]. Among these, *Bletilla striata* polysaccharide (BSP), a glucomannan-type heteropolysaccharide derived from the pseudobulbs of the terrestrial orchid *Bletilla striata*, has been traditionally employed in Chinese medicine for hemostasis, wound healing, and tissue regeneration [21–23]. Structurally, BSP is a hydrophilic polysaccharide primarily composed of mannose and glucose residues [24–26]. Its characteristic triple-helical conformation, stabilized by extensive intermolecular hydrogen bonding via abundant hydroxyl groups, enables the spontaneous formation of hierarchical supramolecular networks [27,28]. This macromolecular architecture confers high mechanical integrity while providing abundant interaction sites for the non-covalent encapsulation of bioactive agents.

Consequently, BSP functions as a self-assembling macromolecular matrix capable of hosting small molecules or phytochemicals without the need for synthetic carriers. Notably, BSP exhibits intrinsic biological activities, including anti-inflammatory, immunomodulatory, and pro-healing effects, which collectively enhance its biomedical relevance by modulating key inflammatory pathways such as NF-κB and MAPK, thereby suppressing the production of pro-inflammatory mediators including NO, IL-6, and IL-1β [29,30]. These multifaceted bioactivities position BSP not merely as an inert carrier but as an active macromolecular component that can synergistically contribute to disease modulation.

Building upon the multifunctional properties of BSP, we further incorporated Dai-Zhe-Shi-San (DZS)—a classical two-herb formulation comprising *Inulae Flos* and Haematitum—as the botanical active component. Within this formula, *Inulae Flos* has been documented in classical Chinese medical texts, including the *Shennong Classic of Materia Medica*, for its efficacy in treating "vomiting" [31]. Modern phytochemical studies have identified sesquiterpenoids and flavonoids as its major bioactive constituents, which exhibit potent anti-inflammatory activities [32]. Mechanistically, *Inulae Flos* extracts suppress the production of pro-inflammatory mediators (NO, IL-6, TNF-α) in LPS-stimulated macrophages via inhibition of NF-κB activation and MAP kinase phosphorylation [33]. Given that chemotherapy-induced neuroinflammation is a key driver of the emetic reflex, this anti-inflammatory action provides a direct pharmacological basis for its traditional antiemetic use and supports its relevance for CINV management [34,35]. Haematitum, the mineral component, is traditionally included to enhance the descending and settling action of the formula. The combination of BSP's intrinsic anti-inflammatory and tissue-repairing properties with DZS's targeted modulation of inflammatory and emetic pathways thus provides a rational basis for developing an integrated, therapeutically active microneedle platform.

Herein, we report a BSP-based dissolving microneedle system that capitalizes on the polysaccharide's dual role as both a structural scaffold and a bioactive matrix. By leveraging the triple-helical supramolecular architecture of BSP, we achieved the spontaneous incorporation of the multi-component DZS formulation without chemical modification, yielding dissolvable microneedles with well-defined geometry. This system addresses the mechanical limitations of conventional dissolving MNs while introducing synergistic therapeutic functionality through the combined anti-inflammatory activities of BSP and DZS. By circumventing gastrointestinal and metabolic barriers, this system establishes a synergistic, dual-action therapeutic mechanism directly at the site of application. This work highlights the potential of bioactive polysaccharides as multifunctional platforms that transcend conventional carrier roles, offering a biomacromolecule-based strategy for integrating traditional herbal actives with modern biomedical interventions.

2. Materials and methods

2.1. Preparation and mechanical strength of BSP@BMNs

BSP (molecular weight: 356.61 ± 49.04 kDa, purity: 98%, batch number: BJDT25, Xi'an Juntai Biotechnology Co., Ltd., China) was dissolved in deionized water at concentrations ranging from 10% to 35% (*w/v*). The solution was hydrated at 4 °C for 24 h and subsequently centrifuged at 3500 rpm for 10 min to remove air bubbles. The resulting BSP solution was then cast into polydimethylsiloxane (PDMS) microneedle molds (10 × 10 array, 800 μm height) using a centrifugal spin coating method to ensure uniform filling of the microcavities. The fabricated BSP-based microneedles (BSP@BMNs) were evaluated for structural integrity in terms of molding fidelity, backing layer uniformity, and morphological completeness, following previously established criteria [36]. To optimize the mechanical performance, BSP@BMNs prepared with 15%, 20%, and 25% (*w/v*) BSP concentrations were subjected to compression testing using a universal mechanical tester (PT-501B, Pusait Instrument, China) at a test speed of 10 mm·min^{-1} and a displacement distance of 720 μm. Force-displacement curves were recorded and analyzed to determine the elastic modulus and fracture strength of the microneedle formulations.

2.2. Preparation and morphological characterization of DZS@BMNs

The DZS formulation, composed of *Inulae Flos* and Haematitum in a

3:1 ratio according to the classical prescription from the Treatise on Exogenous Febrile Disease, was extracted and freeze-dried using optimized protocols [37]. Subsequently, BSP was blended with DZS at mass ratios ranging from 2:1 to 1:4 to prepare homogeneous co-solutions. These solutions were then injected into PDMS micromolds (featuring a 10 × 10 needle array with 800 μm needle height and 200 μm base thickness), followed by centrifugation (3500 rpm, 10 min) and curing under controlled conditions (25 ± 2 °C, 45–55% RH, 24 h) to evaluate backing layer smoothness and drug loading capacity. Morphological characterization was performed through optical microscopy (Nikon ECLIPSE Ts2, Japan) and field-emission scanning electron microscopy (Hitachi TM3000, Japan) with gold-sputtered samples, comparing tip geometry and surface topography between MNs and DZS@BMNs to screen the optimal formulation.

2.3. Evaluation of mechanical properties

DZS@BMNs with varying BSP/DZS mass ratios (2:1–1:2 *w*/w) were subjected to axial compression testing using computer-type single-arm tensile testing machine (Pusait Instrument PT-501B, China). A flat-plate probe compressed individual microneedles at 10 mm·min^{-1} until structural failure, with force-displacement data acquired at 50 Hz sampling frequency.

2.4. Stability evaluation

DZS@BMN ($n = 3$) underwent stability testing in controlled desiccation (25 ± 2 °C, < 20% RH) over 11 days. Chemical integrity of active components was monitored at 48-h intervals using HPLC-UV (Waters e2695, American) with method validation per ICH Q_2 (R_1) (Detection conditions in the supporting information).

2.5. DSC analysis

The calorimetric behavior of the sample solution was studied by DSC (TA Q20, American): pure BSP, DZS extract, physical mixture, DZS@BMNs, and lyophilized BSP gel. Samples (5 ± 0.2 mg) were sealed in aluminum pans and scanned from 40 to 600 °C at 40 °C·min^{-1} under N_2 purge (50 mL·min^{-1}), using empty alumina crucible as reference.

2.6. FT-IR analysis

FT-IR spectra (TENSOR II, Bruker, Germany) were acquired for all material variants (pure BSP, DZS extract, physical mixture, DZS@BMNs, and lyophilized BSP gel) using KBr pellet method (1:200 sample/KBr ratio). Scans covered 4000–400 cm^{-1} range at 4 cm^{-1} resolution with 32 scans per sample, background-corrected against pure KBr reference.

2.7. Transdermal penetration evaluation

Rhodamine 6G-loaded BSP microneedles (R6G-BMNs) were fabricated using a 1 mg·mL^{-1} R6G solution. Both R6G-BMNs and DZS@BMNs were applied to the dorsal dermis of BALB/c nude mice ($n = 3$) with sustained pressure for 10 min to ensure proper insertion. Skin penetration efficacy was systematically evaluated through histological analysis: Tissue samples underwent paraffin embedding, sectioning at 5 μm thickness, and H&E staining, with bright-field microscopy (Nikon TS2, Japan) employed to visualize penetration depth and local tissue response. Parallel validation was performed using Parafilm® sheets (8-layer stacks of 120 μm thickness) as a skin-mimicking substrate to assess the mechanical penetration capability and structural integrity of both BMNs and DZS@BMNs.

2.8. Dermal irritation testing

DZS@BMNs were applied to depilated Wistar rat skin ($n = 6$) for 1 h under occlusive dressing, with contralateral sites as controls. Residual formulation was removed with 37 °C normal saline. Erythema/edema scoring (0–4 scale) was performed at 1, 4, 24, 48, and 72 h post-removal by blinded evaluators using Draize criteria [38].

2.9. Biocompatibility evaluation

L929 fibroblasts were cultured in DMEM with 10% FBS and treated with DZS@BMN (1-500 μg·mL^{-1}) for 24 h. Cell viability was quantified via cell counting kit-8 (CCK-8) assay (MedChemexpress): 10% reagent in medium incubated 2 h, with absorbance measured at 450 nm using a microplate reader (Infinite M 200 NanoQuant, Tecan Trading AG, CH).

Hemocompatibility was evaluated following modified ASTM F756–00 (2000) guidelines. Abdominal aortic blood from anesthetized Wistar rats was diluted with PBS (4:5, *v*/v). Test solutions (500 μg·mL^{-1} in PBS) included DZS extract, DZS@BMNs, BSP, ultrapure water, and PBS. Each sample (10 mL, $n = 5$) was incubated at 37 °C for 30 min, mixed with 200 μL diluted blood, and reintubated for 1 h. post-centrifugation (1500 ×*g*, 5 min), supernatants were transferred to a 96-well plate for OD 545 nm measurement, with macroscopic hemolysis documented photographically. Hemolysis percentage was calculated as follow:

$$\text{Hemolysis Rate } (\%) = [ODa - ODc/ODb - ODc] \times 100\% \quad (1)$$

Where OD_a is the OD of sample, OD_b is the OD of negative control, OD_c is the OD of positive control.

2.10. In vitro release profiling

Neochlorogenic acid, caffeic acid, and 1-*O*-acetylbutylbenzene lactone were selected as marker compounds based on their representativeness as the principal bioactive components derived from *Inulae Flos*, the botanical component of DZS. These components possess well-documented anti-inflammatory activities relevant to the alleviation of CINV and have been established as key quality markers in the chemical profiling of the *Inulae Flos*-Haematitum herb pair [39–41]. Accordingly, monitoring the release kinetics of these compounds enables a pharmacologically relevant assessment of the microneedle delivery system. In vitro release kinetics of neochlorogenic acid, caffeic acid, and 1-*O*-acetylbritannilactone from DZS microneedles were assessed through dynamic dialysis (0.9% saline, 32.0 ± 0.5 °C) using 3.5 kDa RC dialysis bags immersed in 90 mL medium under 100 rpm·min^{-1} agitation. Aliquots (2.0 mL) were collected at scheduled intervals (10–1440 min) with immediate isovolumetric medium replacement, followed by HPLC analysis (Supplementary Materials). Cumulative release profiles were quantified using established calculation models, ensuring continuous sink conditions throughout the 24-h study period [42].

$$Q_n\ (\%) = C_n \times V \times D/W \times 100\% \quad (2)$$

$$Q\ (\%) = Q_n + (Q_1 + Q_2 + Q_{n-1}) \times V_i/V \quad (3)$$

Where Q_n is single-point synthesize degree, Q is the cumulative release, C_n is the concentration of the sample at each point, V is the total volume of dissolution medium, D is the dilution factor, W is the initial drug load, V_i is the sampling volume per time (2 mL).

2.11. In vitro permeation analysis

Full-thickness dorsal skin from euthanized BALB/c nude mice was surgically prepared for Franz cell permeation studies. Microneedle-treated skin (2-min thumb-pressure application) was mounted stratum corneum-up in receptor chambers containing 7 mL pH 7.4 PBS (32.0 ± 0.5 °C, 100 rpm·min^{-1}). Sequential 0.5 mL sampling (2–48 h intervals) with isothermal replenishment preceded 0.22 μm filtration and HPLC quantification of bioactive compounds [43].

$$Q_n = C_n \times V \times D \quad (4)$$

$$Q_n = [Q_n + (Q_1 + Q_2 + \ldots + Q_{n-1}) \times V_i/V] \div S \quad (5)$$

Where Q_n is single-point permeation amount, C_n is the concentration of the sample at each point, V is the total volume of receiving cell, D is the dilution factor, Q is the cumulative permeation, V_i is the sampling volume per time (0.5 mL), S is the effective contact area.

2.12. Anti-inflammatory activity assessment

RAW 264.7 macrophages (2×10^5/well) were treated with: control, LPS (0.2 μg·mL^{-1}), LPS + indomethacin (18 μM), and LPS + DZS@BMN (10–350 μg·mL^{-1}) for 24 h. Centrifuged supernatants (1000 ×*g*, 20 min) were analyzed using Griess assay (Beyotime Biotechnology, China) for NO quantification and ELISA (Thermo Fisher, American) for IL-6/IL-10 detection per manufacturer protocols.

2.13. 5-HT synthesis inhibition in RIN-14B cells

RIN-14B cells (6×10^3/well, 100 μL) were treated with 50 μM LP533401 (positive control) or DZS@BMN solutions (0.01–50 μg·mL^{-1}) in triplicate for 24 h (37 °C, 5% CO_2). Cell viability was assessed via CCK-8 assay (Dalian Meilun Biotechnology Co., Ltd., China), while 5-HT levels in supernatants were quantified using a commercial ELISA kit (Wuhan Gene Beauty Biotechnology Co., Ltd., China) following centrifugation (300 ×*g*, 10 min).

2.14. In vivo pharmacokinetic study

Male Wistar rats weighing 290–310 g were housed under standard laboratory conditions. All animal procedures were approved by the Institutional Animal Ethics Committee (Ethical Review No. TCM-LAEC2024119z1053). After a one-week acclimatization period, the animals were randomly divided into two groups ($n = 6$): an oral administration group and a DZS@BMNs group. Rats in the oral group received a single dose of DZS aqueous extract at a volume of 10 mL·kg^{-1} by oral gavage. In the transdermal group, DZS@BMNs patches were applied to the dorsal skin and left in place until complete microneedle dissolution. At predetermined time points after administration, blood samples were collected from the retinal venous plexus. Plasma concentrations of neochlorogenic acid, a representative bioactive component of DZS, were measured using ultra-performance liquid chromatography coupled with triple-quadrupole mass spectrometry (UPLC-TQ-MS). Detailed chromatographic conditions and mass spectrometric parameters are provided in the Supplementary Materials.

2.15. In vivo 5-HT regulation study

All animal experiments were approved by the Ethics Committee of Tianjin University of Traditional Chinese Medicine (approval No. TCM-LAEC2022072) and were conducted in accordance with institutional guidelines for the care and use of laboratory animals. Male Wistar rats (200 ± 20 g) were housed under a controlled 12 h light/dark cycle with free access to standard chow and water. To establish the pica model, rats were individually housed and acclimatized to kaolin pellets for 72 h before the experiment. The animals were randomly assigned to four groups ($n = 15$): blank control, cisplatin model, dexamethasone (1 mg·kg^{-1}), and DZS@BMNs (human-equivalent dose of 12 g·d^{-1}, adjusted by body weight). On the morning of day 4, 1 h after the final treatment, rats in the cisplatin model, dexamethasone, and DZS@BMNs groups received a single intraperitoneal injection of cisplatin (6 mg·kg^{-1}) to induce pica, while the blank control group received an equivalent volume of saline. Kaolin intake was measured at 12 h intervals after cisplatin injection. To assess the time-dependent effects of the treatments on 5-HT levels, five rats from each group were randomly selected and euthanized at 24 h, 72 h, and 144 h post-cisplatin injection, respectively ($n = 5$). Blood samples, ileum tissues, and whole brain tissues were collected for 5-HT analysis (Wuhan Gene Beauty Biotechnology Co., Ltd., China).

2.16. Rat RNA-sequencing

Cerebral cortex and ileum tissues from experimental groups ($n = 3$) underwent RNA sequencing. Differentially expressed genes (DEGs) were identified using DESeq2 (version 1.40.2; $|\log2FC| > 0.5$, FDR < 0.05) [44]. Functional enrichment analysis employed clusterProfiler (version 4.8.3) for GO terms and KEGG pathways. Gene Set Variation Analysis (GSVA, version 1.48.3) quantified pathway activity [45]. Bioactive DZS@BMN components were screened via TCMSP database (OB $\geq$ 30%, DL $\geq$ 0.18), with network pharmacology analysis conducted on TCMNP platform (version 0.1.0). Spearman correlations ($|\rho| > 0.3$, $P < 0.05$) linked target genes to neuroinflammatory/neurotransmitter markers [46].

2.17. Statistical analysis

All data are presented as mean ± standard deviation (SD) from at least three independent experiments. Transcriptomic data analyses were conducted using R (version 4.1.2) with relevant Bioconductor packages. For statistical comparisons, differences between two groups were assessed using either Student's *t*-test (for parametric data) or the Mann-Whitney *U* test (for non-parametric data). For multiple group comparisons, ANOVA followed by Tukey's post-hoc test was employed. All statistical tests were performed using SPSS 25.0 (IBM), and graphical representations were generated using GraphPad Prism 9.0. Statistical significance was set at $^*p < 0.05$.

3. Results and discussion

3.1. Preparation and transdermal performance of BMNs

To fabricate the microneedles, a 15% (*w/v*) BSP solution was selected as the optimal formulation. This concentration consistently yielded uniform quadrangular pyramidal structures (Fig. 1a). The resulting microneedles exhibited sufficient mechanical strength to penetrate Parafilm® (Fig. S1). Optical microscopy and SEM imaging further confirmed the structural integrity of the microneedles. No signs of bending, warping, or deformation were observed. These findings indicate that the formulation provides adequate mechanical support for skin insertion without compromising structural stability. Following in vivo application, the microneedles formed well-defined 10 × 10 microarrays on murine skin (Fig. 1b). CLSM analysis revealed a penetration depth of 180 ± 12 μm (Fig. 1c), confirming successful traversal of the stratum corneum. This measured depth aligns with previous reports demonstrating that microneedles ranging from 150 to 300 μm in length can effectively cross the stratum corneum while minimizing dermal nerve stimulation [47,48]. Consequently, such dimensions enable efficient transdermal delivery with reduced pain perception. Dissolution studies indicated that approximately 50% of the microneedle material dissolved within 30 min of insertion. Near-complete dissolution was achieved by 120 min (Fig. 1d). This rapid dissolution profile supports bolus release of the therapeutic payload into the dermal microcirculation. It facilitates a fast onset of action and obviates the need for post-application needle removal. These characteristics are consistent with the established advantages of dissolving microneedles as a patient-friendly delivery platform [49].

3.2. Structural characterization of DZS@BMNs

We systematically evaluated the mechanical integrity of DZS@BMNs across a range of BSP-to-DZS mass ratios. A 1:2 ratio (BSP: DZS) was

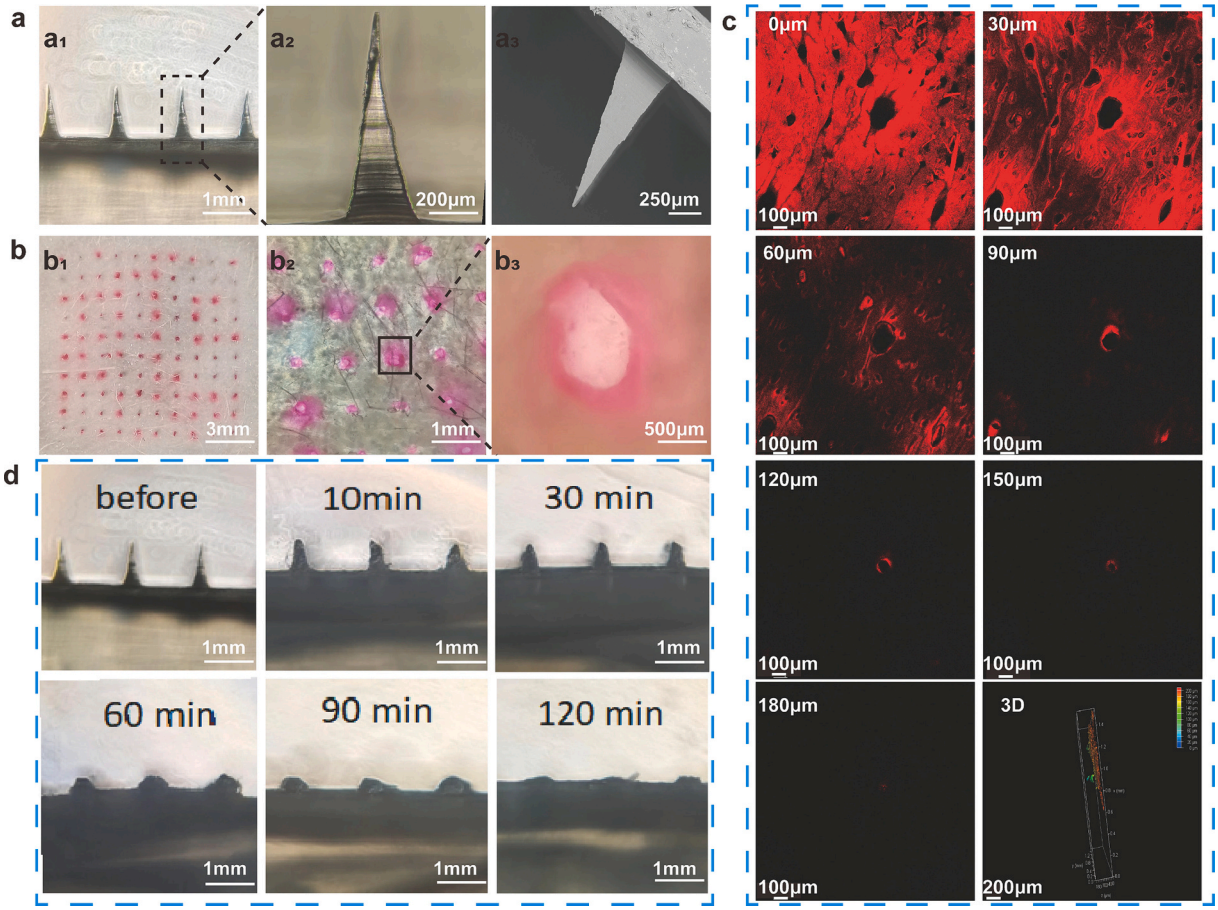

Fig. 1. Morphology and transdermal performance of BMNs. (a) Optical microscopy images of BMNs showing (a_1) top view, (a_2) side view, and (a_3) magnified side view captured by SEM. (b) Skin insertion of R-6G-loaded BMNs presented as (b_1) digital photograph of the inserted skin, (b_2) microscopic image of the insertion site, and (b_3) magnified microscopic image of the insertion site. (c) Representative CLSM image showing the percutaneous penetration of R-6G from BMNs into mouse skin. (d) Dissolution profile of BMNs in mouse skin.

identified as optimal, achieving a balance between drug loading and structural stability, as reflected by consistent force-displacement profiles (Fig. 2c and S2). This improvement in mechanical strength is attributed to the formation of interchain hydrogen bonds and secondary associations within the BSP network during solvent evaporation, which reinforce the matrix without requiring additional crosslinkers.

Unlike conventional microneedle matrix materials such as polyvinyl alcohol, polyvinylpyrrolidone, or hyaluronic acid, which often require chemical crosslinkers or plasticizers to balance mechanical integrity and release performance, BSP is a naturally derived biomacromolecular polysaccharide that forms a self-supporting network through physical entanglement and hydrogen bonding via its abundant hydroxyl and carboxyl groups [50–52]. This eliminates the need for exogenous crosslinking agents, thereby avoiding potential cytotoxicity or inactivation of heat-sensitive botanical components. Notably, although skin barrier properties vary with age, with older individuals exhibiting increased stratum corneum stiffness and reduced barrier recovery, dissolving microneedles can be adapted across age groups by adjusting parameters such as needle length, insertion speed, tip geometry, and material stiffness, ensuring effective penetration without increased tissue damage [53,54].

DZS@BMNs retained the pyramidal morphology of blank MNs (Fig. 2a). Parafilm® penetration tests confirmed enhanced delivery of the active pharmaceutical ingredients (APIs) to deeper skin layers (536–670 μm), indicating improved mechanical integrity and transdermal insertion capability (Fig. 2b and S3). This penetration depth exceeds the thickness of the stratum corneum (approximately 10–20 μm) and reaches the viable epidermis and upper dermis, a range considered favorable for systemic absorption of macromolecular or poorly permeable drugs [55].

DSC and FT-IR analyses confirmed the physical encapsulation of DZS within the BSP helical matrix. In the DSC thermogram, the characteristic endothermic peak of BSP at 94.7 °C was retained in the physical mixture but disappeared in the DZS@BMNs formulation, indicating that DZS components were embedded within the BSP network, thereby altering the thermal behavior of the polysaccharide matrix (Fig. 2e). FT-IR analysis showed that the characteristic absorption bands of BSP, including those at 897.55 and 884.20 cm^{-1} (assigned to the C—H bending vibration of the β-anomeric configuration of mannose) remained unchanged in the DZS@BMNs formulation, while no new peaks indicative of covalent crosslinking were observed (Fig. 2d). Together, these results support the formation of non-covalent interactions between BSP and the active constituents of DZS, without chemical modification of either component. This helical conformation creates a protective microenvironment for the encapsulated botanical constituents, allowing BSP to function not merely as a structural scaffold but as an active stabilizer that preserves the native structure and bioactivity of the loaded ingredients. H&*E*-stained skin sections following MN application (Fig. 3a) showed intact epidermal layers surrounding discrete microchannels (180 μm), demonstrating consistent penetration and no signs of an inflammatory response.

Collectively, these findings indicated that BSP-based microneedles effectively integrate botanical formulations through physical encapsulation, maintain structural homogeneity, and possess sufficient

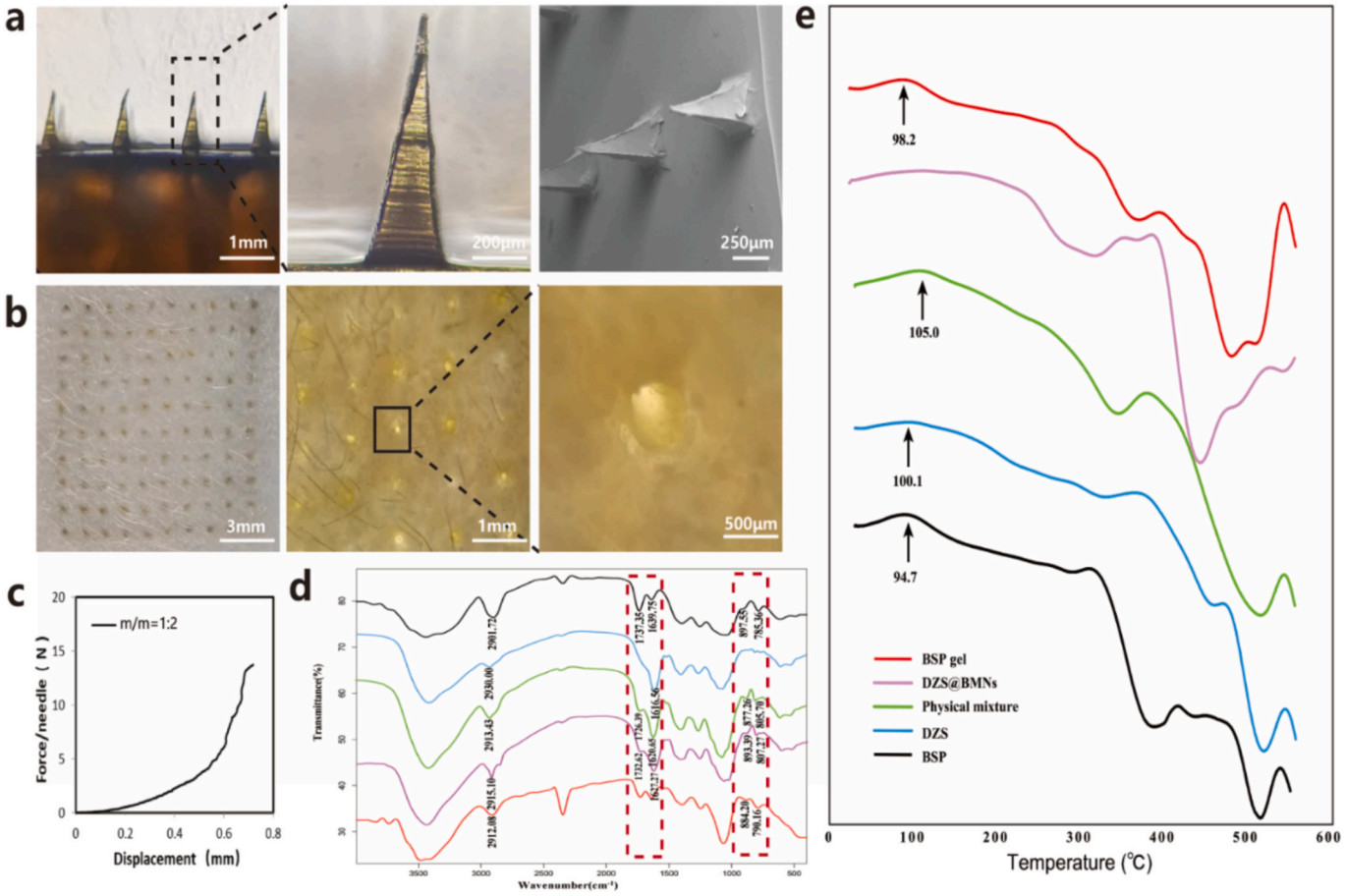

Fig. 2. Structural and mechanical characterization of DZS@BMNs. (a) OM and SEM images of DZS@BMNs. (b) Microscopic images of skin puncture of DZS@BMNs. (c) Mechanical strength (force-displacement curve) of DZS@BMNs. (d) FT-IR spectra of BSP gel, DZS@BMNs, DZS and BSP physical mixture, DZS, BSP. (e) DSC thermograms of BSP gel, DZS@BMNs, DZS and BSP physical mixture, DZS, BSP.

mechanical robustness for minimally invasive administration, positioning them as a distinctive platform that combines the advantages of naturally derived biomacromolecules with the functional versatility of microneedle technology for transdermal delivery of natural product-based therapeutics.

3.3. Biocompatibility of DZS@BMNs

We systematically assessed the biosafety of DZS@BMNs through dermal irritation, cytocompatibility, and hemocompatibility assays. Upon application, the microneedles generated a 10 × 10 array of transient microchannels in the skin (Fig. 3c, 0 min), an inherent consequence of physical penetration. These micropores closed rapidly, with skin recovery observed within 60 min post-application (Fig. 3c), confirming the transient nature of the micro-injuries. Throughout the observation period, no visible erythema, edema, or microlesion was observed at the application sites (mean irritation score = 0; Fig. 3a). The microneedles fully dissolved within 90 min (Fig. S4), correlating with the rapid micropore closure kinetics. Cytotoxicity assays using L929 fibroblasts demonstrated cell viability exceeding 90% even at the highest tested concentrations (10 mg mL^{-1} BSP or 500 μg mL^{-1} DZS@BMNs) (Fig. 3d-3f). Hemolysis remained below 2%, well within the ISO 10993-4 safety limit (Fig. 3g, h), indicating excellent erythrocyte compatibility and no membrane disruption. To evaluate formulation stability, DZS@BMNs were stored under ambient conditions (25 °C, 20% RH) for 11 days. The API content remained above 97% (RSD < 3%), indicating that the BSP matrix effectively protected the botanical compounds from oxidative or hydrolytic degradation during storage (Table S1). The complete and rapid skin restoration within 60 min post-application, combined with the absence of dermal irritation and robust cytocompatibility, demonstrates that repeated DZS@BMNs administration does not induce cumulative tissue damage, thereby supporting its safety profile for long-term intermittent use in CINV management.

Clinically, patients receiving CINV-associated chemotherapy are predominantly older adults. According to the American Cancer Society, 88% of cancer diagnoses occur in individuals aged 50 years or older, and 59% in those aged 65 years or older. Treatment rates among younger patients have increased by 11.7% from 2020 to 2023, highlighting the need for strategies effective across all ages. Although the present data were obtained in animal models, the comprehensive safety profile supports the translational feasibility of DZS@BMNs for human application.

3.4. In vitro release and permeation analysis of DZS@BMNs

In vitro release studies showed that DZS@BMNs exhibited a biphasic pattern, with an initial rapid phase within the first 2 h (cumulative release of 40–50% for all three components), followed by a sustained phase exceeding 90% release by 24 h (Fig. 3i). The release kinetics followed a first-order model ($R^2 > 0.98$; Table S2), consistent with a concentration-dependent diffusion process. In vitro skin permeation studies using Franz diffusion cells revealed progressive accumulation of all three compounds over 48 h. Cumulative permeation reached 14.2 ± 2.6% (neochlorogenic acid), 5.6 ± 1.2% (caffeic acid), and 11.4 ± 1.5% (1-*O*-acetylbritannilactone) at 24 h, increasing to 18.3 ± 1.8%, 8.6 ± 1.5%, and 23.9 ± 2.2%, respectively, by 48 h (Fig. 3j). This delivery profile is achieved through a dual-phase mechanism. Initially, the

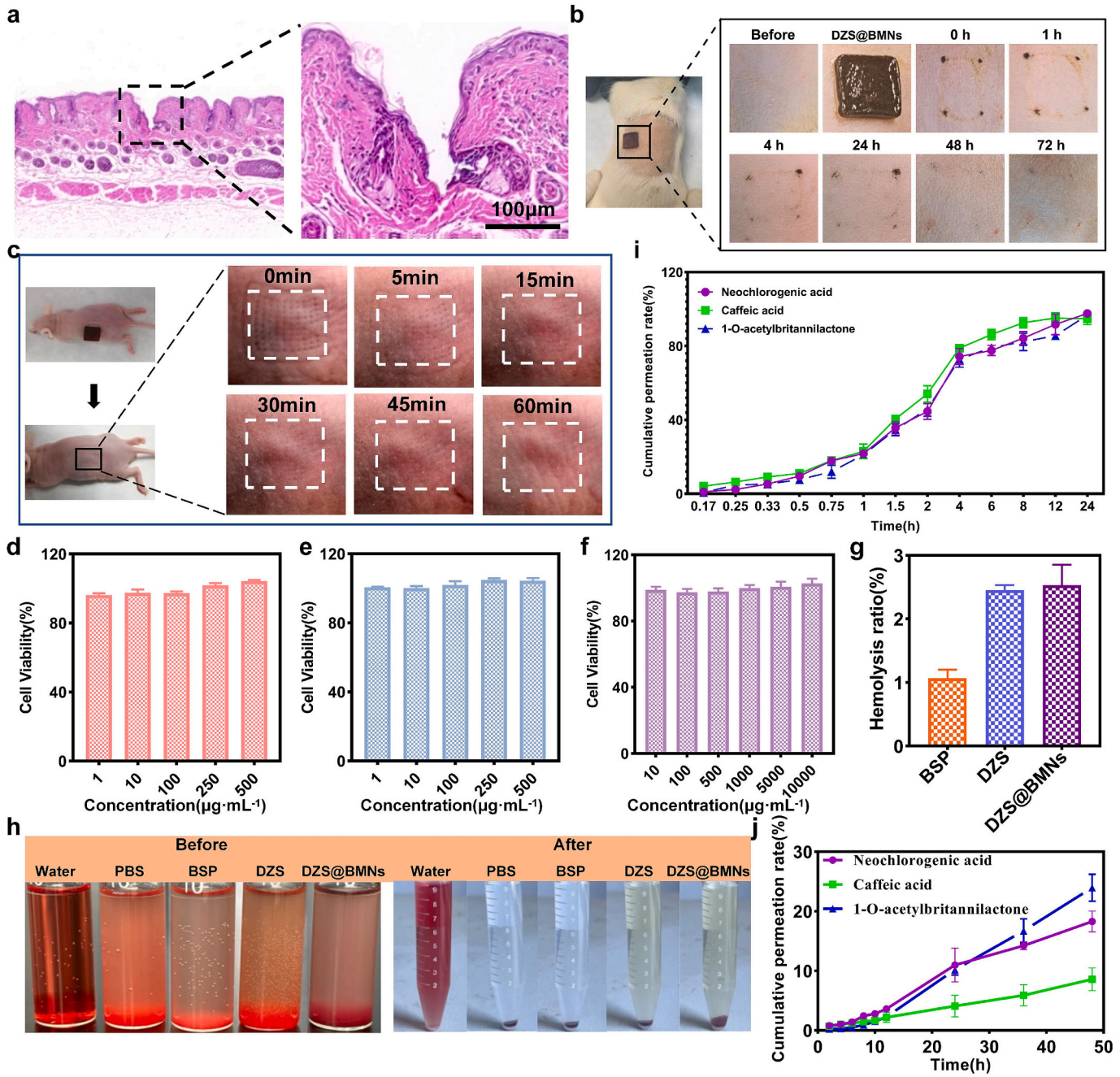

Fig. 3. Biocompatibility and in vitro transdermal characterization of DZS@BMNs. (a) H&*E*-stained photomicrographs of skin sections at the application sites of DZS@BMNs. (b) Skin irritation scores (0–72 h post-application). (c) Time-dependent skin restoration after DZS@BMNs application. (d) Cell viability of L929 fibroblasts treated with varying concentrations of DZS ($n = 3$). (e) Cell viability of L929 fibroblasts treated with varying concentrations of DZS@BMNs ($n = 3$). (f) Cell viability of L929 fibroblasts treated with varying concentrations of BSP ($n = 3$). (g, h) Hemolysis percentages of BSP, DZS, and DZS@BMNs ($n = 3$). (i) Cumulative in vitro release profiles of three marker components from DZS@BMNs over 24 h. (j) Cumulative in vitro permeation profiles of three marker components from DZS@BMNs through rat skin over 48 h ($n = 3$).

microneedles create microchannels approximately 180 μm in depth within the stratum corneum, establishing transient pathways that facilitate drug penetration. Rapid tip dissolution occurs within 90 min, enabling immediate diffusion of the active pharmaceutical ingredients. Subsequently, the backing reservoir serves as a prolonged permeation source, maintaining a sustained concentration gradient that drives continued delivery through the established microchannels over 48 h. The time-dependent increase in permeation, particularly after 12 h, correlates with the sustained release phase, indicating that continuous drug release from the reservoir supports prolonged transdermal flux. Together, this dual-mode mechanism enables rapid onset and sustained delivery of botanical active ingredients.

3.5. *Pharmacokinetic analysis of DZS@BMNs*

To evaluate the systemic exposure profile of DZS@BMNs and to clarify the intended therapeutic pathway, we performed a comparative pharmacokinetic study in rats. Neochlorogenic acid was selected as the marker compound for pharmacokinetic analysis based on its established role as a quality marker of *Inulae Flos*. As such, its plasma concentration profile serves as a reliable indicator of systemic absorption of the DZS components following transdermal administration. Following a single

administration, plasma concentrations of neochlorogenic acid were measured at designated time points using UPLC-TQ-MS. As shown in Fig. 4, both the oral DZS solution and the DZS@BMNs transdermal system achieved a peak concentration (T_{max}) at 15 min post-administration. It indicated that the transdermal route enabled rapid drug entry into the systemic circulation, effectively bypassing the delayed absorption commonly associated with oral administration due to gastric emptying and variable intestinal transit. The C_{max} of neochlorogenic acid was 295.1 ng·mL^{-1} in the DZS@BMNs group, markedly higher than the 190.0 ng·mL^{-1} observed in the oral group ($p < 0.01$). This 55% increase in C_{max} suggests that transdermal delivery achieves a higher peak systemic exposure compared with oral administration. Furthermore, the AUC for DZS@BMNs was increased by 9.3% for $AUC_{0–24h}$ and by 11.5% for $AUC_{0-\infty}$ relative to the oral group. These improvements in systemic exposure can be attributed to the ability of the DZS@BMNs platform to circumvent first-pass hepatic metabolism and gastrointestinal degradation.

Collectively, the pharmacokinetic data provide direct evidence that DZS@BMNs achieves systemic delivery of active components. The rapid absorption profile ensures timely intervention during the acute phase of CINV, while the enhanced C_{max} and AUC values confirm improved bioavailability relative to the conventional oral route. Importantly, these findings substantiate the intended therapeutic pathway of the DZS@BMNs system: transdermal administration enables the active constituents to enter systemic circulation and subsequently exert their pharmacological effects on both peripheral targets and central targets.

3.6. *In vivo evaluation of anti-emetic efficacy in cisplatin-induced CINV models*

We evaluated the antiemetic efficacy of DZS@BMNs using a cisplatin-induced pica model, a well-established surrogate for CINV. This model mimics CINV-like behaviors through central serotonergic activation, with increased kaolin intake serving as a widely accepted indirect measure of nausea in rodents [56,57]. Cisplatin produced a significant and sustained increase in kaolin consumption relative to controls, confirming successful model establishment (Fig. 5a-5b). As shown in Fig. 5b, DZS@BMNs significantly reduced kaolin intake during the 24–108 h period after cisplatin administration compared with the model group. The cisplatin-induced pica model is characterized by an acute phase (0–24 h), driven primarily by 5-HT_3R activation, and a delayed phase (> 24 h), which involves NK_1R signaling and inflammatory pathways [58]. At the 24-h mark, corresponding to the acute phase, DZS@BMNs reduced kaolin intake by 38% relative to the dexamethasone group (1.30 g vs 0.81 g). This degree of acute-phase suppression carries clinical significance, since poor early emesis control is a known predictor of delayed-phase CINV and anticipatory nausea in later chemotherapy cycles [59]. Dexamethasone produced greater reductions in kaolin consumption during the delayed phase, a finding consistent with its well-documented anti-inflammatory effects in later-stage emesis [60]. Its acute-phase activity, however, is comparatively limited when measured against agents that directly interfere with serotonergic transmission. In contrast, DZS@BMNs acts by inhibiting serotonin biosynthesis, thereby providing strong antiemetic protection during the acute phase. It is worth noting that the efficacy of both ondansetron and dexamethasone may become limited upon repeated administration. DZS@BMNs, a transdermal system based on a clinically validated botanical formulation, represents a well-tolerated and noninvasive alternative in settings where conventional antiemetic options offer suboptimal benefit.

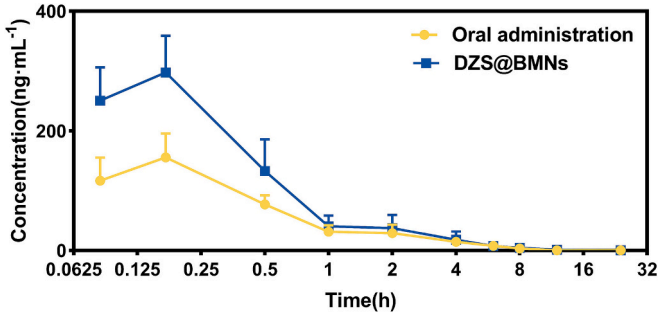

Fig. 4. Pharmacokinetic results in rats ($n = 6$).

Mechanistically, treatment with DZS@BMNs resulted in tissue-specific reductions in 5-HT levels across key components of the gut-brain axis, with decreases of 42% in the brain ($p < 0.01$), 38% in the ileum ($p < 0.05$), and 22% in plasma relative to the model group (Fig. 5c-5e). These findings indicate that BSP-mediated transdermal delivery of the botanical formulation is associated with reduced 5-HT levels in both peripheral and central compartments. Notably, the reduction in 5-HT levels closely paralleled the observed behavioral improvements, suggesting that suppression of serotonergic hyperactivity is a key mechanism underlying the antiemetic efficacy of DZS@BMNs. Together, these results suggest that DZS@BMNs exerts potent antiemetic effects, with concurrent reductions in central and peripheral serotonin levels closely paralleling the observed behavioral improvements. Although a BSP-BMNs control was not included, as the study focused on the integrated DZS@BMNs system, the anti-inflammatory properties of BSP are well established, particularly through the inhibition of NF-κB and NLRP3 pathways [61,62]. In our LPS-stimulated RAW264.7 macrophages, BSP also showed potent suppression of NO and IL-6 along with restoration of IL-10 (Fig. 7e-7g). H&E staining also confirmed the efficacy of DZS@BMNs (Fig. 5f).

3.7. *Transcriptomic assessment into neuroimmune modulation*

To elucidate the molecular mechanisms underlying the anti-emetic efficacy of DZS@BMNs, transcriptomic profiling was performed on brain and ileal tissues. These sites were selected because they represent the two principal hubs of the gut-brain axis that orchestrate 5-HT and cytokine-mediated neuroimmune signaling during CINV. The brainstem (area postrema and nucleus tractus solitarius) acts as a central vomiting center, while the ileum serves as the major peripheral source of 5-HT release. This dual-tissue strategy allows parallel assessment of central and peripheral responses to BSP-based microneedle intervention.

Comparative transcriptomic analysis revealed that cisplatin induced extensive transcriptional perturbations, with 810 differentially expressed genes (DEGs; 185 upregulated, 625 downregulated) in brain tissue and 2003 DEGs (1514 upregulated, 489 downregulated) in ileum compared with the control group (Fig. 6a-6b). Treatment with DZS@BMNs markedly reversed these alterations, yielding 5554 DEGs (2321 upregulated, 3233 downregulated) in brain and 1088 DEGs (609 upregulated, 479 downregulated) in ileum versus the model group. In contrast, dexamethasone treatment modulated only 627 DEGs in brain and 847 DEGs in ileum, suggesting that the macromolecular formulation induced broader transcriptomic reprogramming.

GO enrichment analysis revealed that the DEGs regulated by DZS@BMNs were significantly enriched in biological processes related to neurotransmitter secretion, calcium ion-regulated exocytosis, synaptic transmission, and inflammatory response (Fig. 6c-6d). These results implied a coordinated restoration of synaptic homeostasis and neuroimmune balance. KEGG pathway enrichment further indicated activation of oxytocin, Ras, and MAPK signaling pathways (Fig. 6e-6f), which were known to modulate both neuronal excitability and cytokine release. Together, these transcriptomic signatures suggested that DZS@BMNs re-established cross-talk between serotonergic and inflammatory networks disrupted by cisplatin exposure. Pharmacological target mapping identified 308 potential molecular interactors, among which Gabrp, Cyp3a2, Car3, and Mpo were strongly correlated with IL-6 and TNF-α expression levels (Fig. S5-S16). This highlights a potential

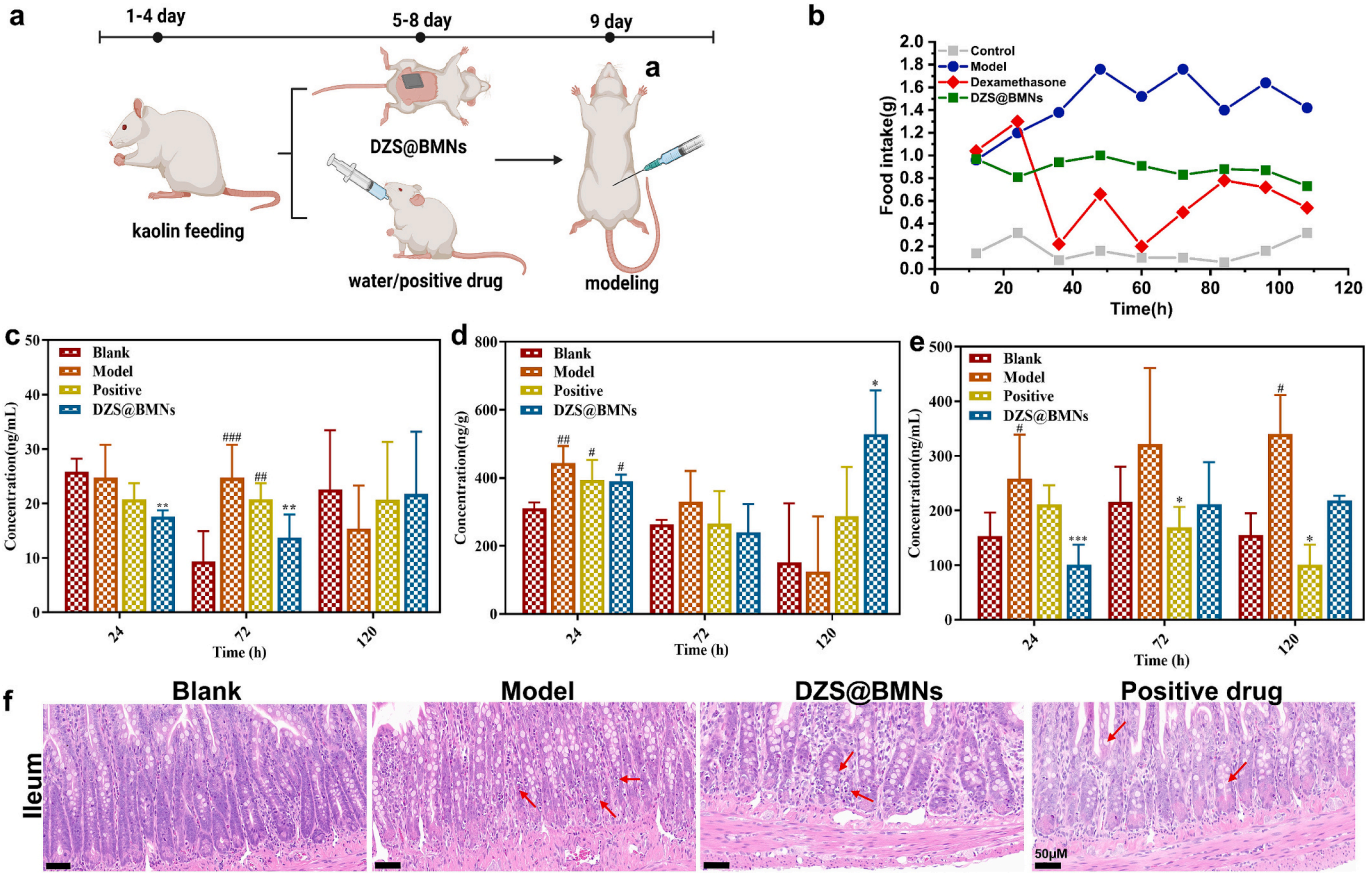

Fig. 5. In vivo anti-emetic efficacy of DZS@BMNs in cisplatin-induced CINV models. (a) Schematic illustration of the experimental design. (b) Time-dependent kaolin consumption in each treatment group over 120 h following cisplatin administration. (c-e) 5-HT levels in brain tissue (c), ileal tissue (d), and plasma (e). (f) Representative images of H&E staining in each group of rats. Data are expressed as mean ± SD ($n = 5$). Statistical analysis was performed by one-way ANOVA followed by Tukey's post hoc test. $^{\#}p < 0.05$, $^{\#\#}p < 0.01$, and $^{\#\#\#}p < 0.001$ indicate significant differences compared to the model group.

dual regulatory mechanism-attenuation of pro-inflammatory cytokine expression and downregulation of excitatory neurotransmission-both contributing to the observed anti-emetic effect.

Mechanistically, DZS@BMNs modulated tissue-specific neuro-immune signatures along the gut-brain axis. In brain tissue, both DZS@BMNs and dexamethasone suppressed cisplatin-induced over-expression of Tph1 and Drd1, while DZS@BMNs exerted a stronger inhibitory effect on neuroinflammatory markers such as IL-6 and NF-κB. In ileal tissue, the microneedle treatment reduced the expression of Th, Drd2, and 5-HT_3R subunits, while concomitantly suppressing IL-1β, IL-6, and TNF-α transcripts, demonstrating synchronized inhibition of neurotransmitter biosynthesis and inflammatory cascades (Fig. 6g-6i).

Collectively, the transcriptomic data indicate that DZS@BMNs exert a bidirectional regulatory effect on neuroimmune interactions along the gut-brain axis. This is achieved through the concurrent suppression of serotonergic and dopaminergic signaling, alongside the inhibition of cytokine-mediated inflammatory responses. Given the exploratory nature of transcriptomic analysis, these findings should be interpreted as hypothesis generating. They provide a foundational molecular framework that requires further functional validation to establish the causal mechanisms underlying the anti-emetic effects of DZS@BMNs.

3.8. In vitro anti-inflammatory

To evaluate the anti-inflammatory efficacy of DZS@BMNs, we established an LPS-induced macrophage model using RAW 264.7 cells. In LPS-stimulated RAW 264.7 cells, treatment with DZS@BMNs (350 μg·mL^{-1}) significantly reduced NO production by 60.2% ($p < 0.001$) and decreased IL-6 levels by 99.0% ($p < 0.001$) compared to the model group. Additionally, DZS@BMNs partially restored IL-10 to 31.30 ± 11.61 pg·mL^{-1} ($p < 0.001$), reaching 94.4% of the baseline level and reversing the 2.1-fold increase induced by LPS. Notably, DZS@BMNs outperformed indomethacin, a first-line anti-inflammatory drug, in modulating these inflammatory mediators (Fig. 7a-7h). Collectively, these findings demonstrate that DZS@BMNs exerts potent anti-inflammatory effects by suppressing pro-inflammatory factors and restoring the balance of anti-inflammatory cytokines, highlighting its therapeutic potential for inflammation-related conditions such as CINV.

3.9. Biosynthesis inhibition of 5-HT by DZS@BMNs

As first-line therapeutic agents for the management of CINV, 5-HT_3R antagonists exerted potent antiemetic effects by selectively inhibiting the binding of 5-HT to 5-HT_3R [63–65]. RIN-14B cells, which share close phenotypic and functional homology with enterochromaffin-cells (EC) (including the expression of TPH1 and chromogranin A, as well as stimulus-evoked 5-HT release), serve as a well-validated in vitro model for investigating EC-lie serotonin biosynthesis and secretion [66]. The half-maximal inhibitory concentration (IC_{50}) of DZS@BMNs on RIN-14B cell viability was 0.29 mg·mL^{-1}, indicating a favorable safety window for subsequent functional assays. Using this model, we found that DZS@BMNs suppressed 5-HT secretion in a concentration-dependent manner. At 50 μM, DZS@BMNs reduced serotonin output to 44.54 ± 0.84 ng·mL^{-1}, outperforming the selective TPH1 inhibitor LP533401 (68.73 ± 0.86 ng·mL^{-1}, $p < 0.001$, Fig. 7i-7j). This finding suggests that botanical formulations can achieve more potent inhibition of peripheral serotonin synthesis than single-target inhibitors, potentially through synergistic modulation of multiple pathways involved in TPH1

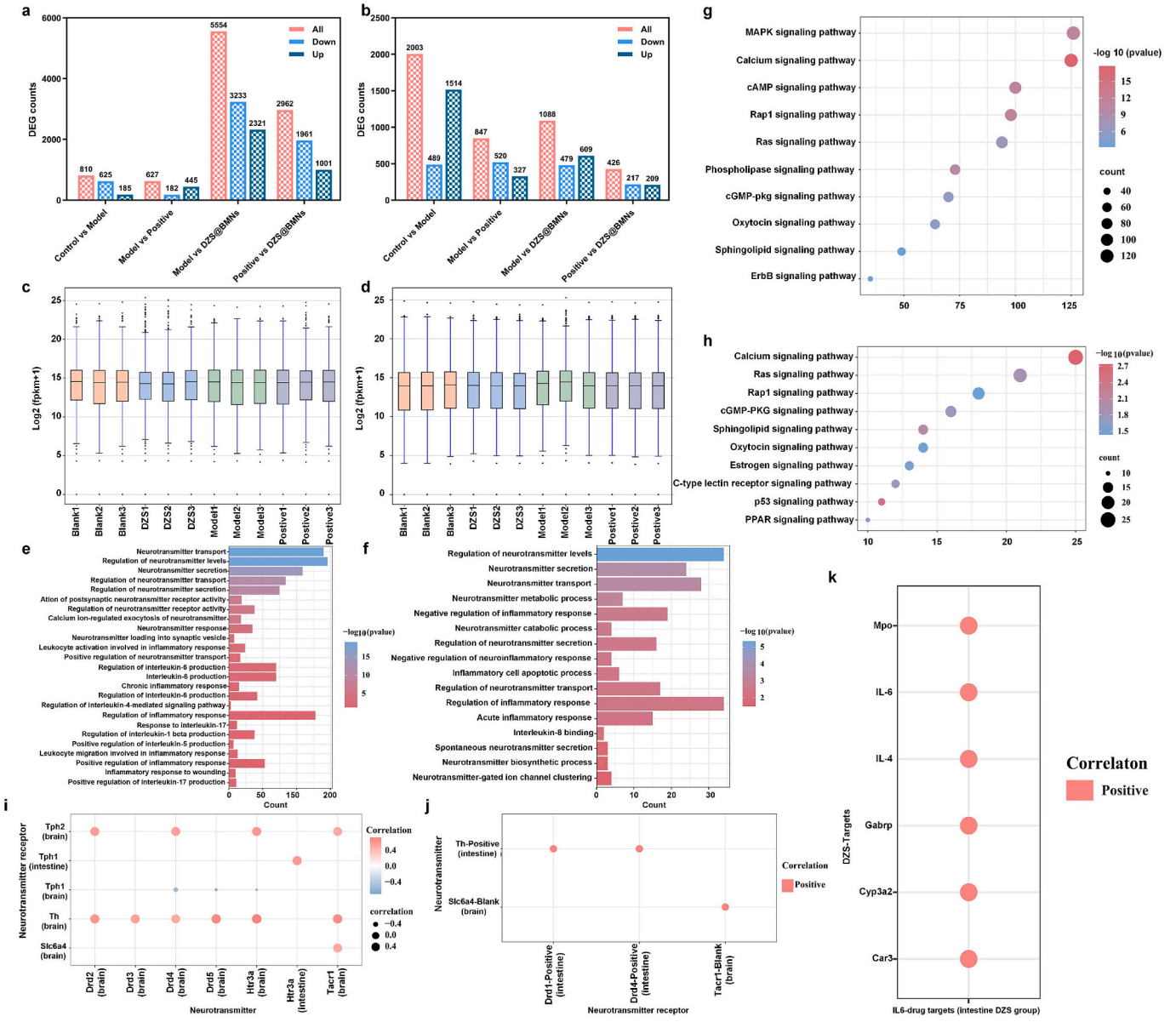

Fig. 6. Transcriptomic dissection of DZS@BMNs-mediated neuroimmune modulation. (a) Number of DEGs identified in brain tissue. (b) Number of DEGs identified in ileal tissue. (c-d) Genome-wide expression profiles displayed as boxplots showing median, quartiles, and 1.5 × interquartile range (IQR) in brain (c) and ileum (d). (e) GO enrichment analysis of DEGs in brain. (f) GO enrichment analysis of DEGs in ileum. (g) KEGG pathway enrichment analysis of DEGs in brain. (h) KEGG pathway enrichment analysis of DEGs in ileum. (i-k) Correlation networks linking neurotransmitter receptor-encoding genes, neurotransmitter-encoding genes, and inflammatory cytokine-encoding genes to DZS@BMNs treatment targets ($n = 3$).

expression and activity.

Collectively, these results indicated that DZS@BMNs acts upstream of receptor blockade by directly inhibiting serotonin biosynthesis, thereby interrupting the emetic cascade at its source. This biosynthetic targeting offers a mechanistic advantage over conventional 5-HT_3 receptor antagonists, which only interfere with downstream receptor signaling, and positions DZS@BMNs as a promising multimodal strategy for managing refractory CINV, particularly in cases where receptor antagonists alone provide inadequate control. This biosynthetic mechanism is closely tied to the properties of the delivery system itself. The ability to achieve such pharmacological effects is enabled by the choice of BSP as the microneedle matrix. Unlike conventional microneedle substrates such as synthetic polymers or hyaluronic acid, which serve predominantly as inert structural materials, BSP is a naturally derived biomacromolecule that contributes beyond mechanical support. It exhibits intrinsic biocompatibility, enables physical encapsulation of labile botanical components without covalent modification, and maintains formulation stability during storage. In the present system, BSP thus functions as an integral component that supports both the integrity and the activity of the loaded formulation. This integration of material functionality with therapeutic design distinguishes the present biomacromolecular microneedle approach from existing transdermal platforms.

A schematic overview of the proposed mechanism is provided in Fig. 8. Transdermal dministration of DZS@BMNs enables coordinated neuroimmune modulation along the gut-brain axis: peripheral suppression of serotonin biosynthesis and inflammation, coupled with central attenuation of neuroinflammation and modulation of serotonergic and dopaminergic signaling. This dual-pathway regulation, supported by the multifunctional BSP matrix, interrupts the emetic cascade at multiple levels.

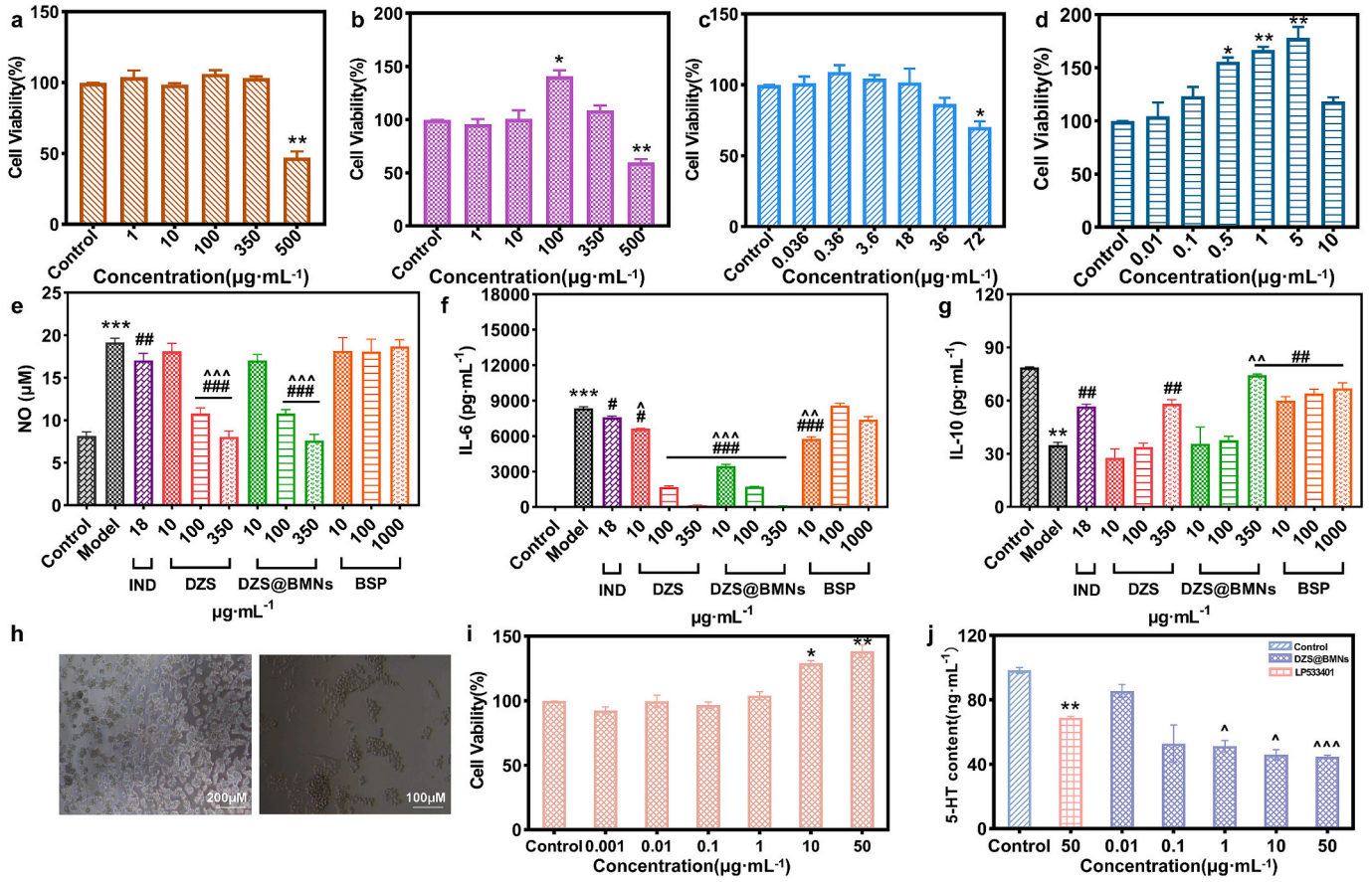

Fig. 7. Dual-pathway anti-emetic effect of DZS@BMNs in vitro. (a) Cell viability of RAW 264.7 cells treated with various concentrations of DZS. (b) Cell viability of RAW 264.7 cells treated with various concentrations of DZS@BMNs. (c) Cell viability of RAW 264.7 cells treated with various concentrations of IND. (d) Cell viability of RAW 264.7 cells treated with various concentrations of BSP. (e) NO production in RAW 264.7 cells after different treatments. (f) IL-6 levels in RAW 264.7 cells after different treatments. (g) IL-10 levels in RAW 264.7 cells after different treatments. (h) Representative morphology images of RAW 264.7 macrophages under treatment with LPS (0.001 μg·mL^{-1}) and DZS@BMNs. (i) Cell viability of RIN-14B cells treated with various concentrations of DZS@BMNs. (j) 5-HT secretion levels in RIN-14B cells after treatment with various concentrations of DZS@BMNs. Data are expressed as mean ± SD values ($n = 3$). Statistical analysis was performed by one-way ANOVA followed by Tukey's post hoc test. $^{*}p < 0.05$, $^{**}p < 0.01$ and $^{***}p < 0.001$ indicate significant differences compared to the control group; $^{\#}p < 0.05$, $^{\#\#}p < 0.01$ and $^{\#\#\#}p < 0.001$ indicate significant differences compared to the model group; $\hat{}p < 0.05$, $\hat{}\hat{}p < 0.01$ and $\hat{}\hat{}\hat{}p < 0.001$ indicate significant differences compared to the IND or LP533401 group.

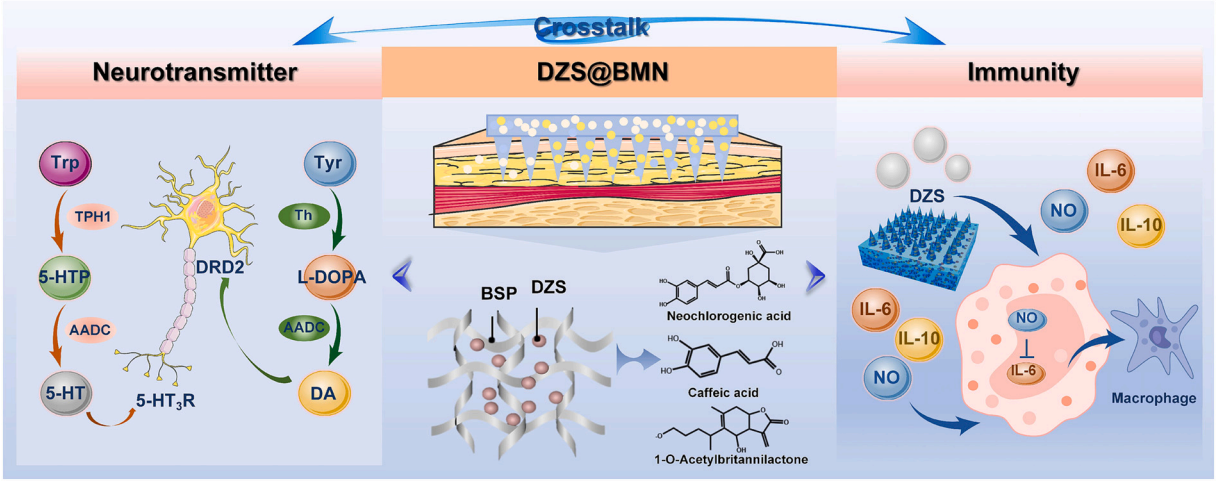

Fig. 8. DZS@BMNs-mediated neuroimmune modulation along the gut–brain axis. The BSP-based microneedle platform bypasses hepatic first-pass metabolism and enables direct systemic delivery of bioactive constituents. In the periphery, the system suppresses ileal 5-HT biosynthesis and attenuates pro-inflammatory mediators NO and IL-6. Central neurotransmitter homeostasis is restored through reduced brain 5-HT content and downregulation of Th and DRD2. Peripheral inflammatory suppression and central neurochemical normalization operate as a coupled bidirectional circuit, defining a core mechanistic axis of the observed antiemetic activity.

4. Conclusion

In this study, we developed BSP-based microneedles (DZS@BMNs) as a carrier-free macromolecular platform that utilizes the intrinsic bioactivity of the natural polysaccharide BSP to integrate multi-component botanical therapeutics for the management of CINV. This system modulated serotonergic and dopaminergic signaling while suppressing pro-inflammatory cytokine cascades, thereby achieving bidirectional neuroimmune regulation along the gut-brain axis. As a biomacromolecule, the BSP matrix not only provided structural integrity and physical encapsulation of labile botanical components but also contributed to the overall anti-inflammatory effect. Its biodegradable architecture enabled rapid skin penetration and sustained drug release without gastrointestinal toxicity, supported by favorable biosafety profiles and inherent mucosal-protective properties. Overall, DZS@BMNs represent an innovative carrier-free microneedle system with notable advantages and potential for CINV treatment, offering a novel and effective therapeutic strategy. While the robust efficacy of DZS@BMNs in preclinical models supports its considerable promise for CINV management, the inherent complexity of multi-component botanical formulations will necessitate substantial investments in both time and financial resources to advance the system through rigorous pharmaceutical development and clinical translation.

List of abbreviations

APIs	Active pharmaceutical ingredients
BSP	*Bletilla striata* polysaccharide
CCK-8	Cell counting kit-8
CINV	Chemotherapy-induced nausea and vomiting
DZS	Dai-Zhe-Shi-San
EC	Enterochromaffin cells
MN	Microneedle
PDMS	Polydimethylsiloxane
UPLC TQ MS	Ultra performance liquid chromatography coupled with triple quadrupole mass spectrometry

CRediT authorship contribution statement

Lihua Tan: Writing – original draft, Software, Methodology, Data curation, Conceptualization. **Yi Liu:** Supervision, Project administration, Conceptualization. **Zhongli Jing:** Methodology, Data curation, Conceptualization. **Rui Zhu:** Software, Methodology, Data curation. **Xinhui An:** Software. **Giulia Vanti:** Investigation. **Anna Rita Bilia:** Writing – review & editing. **Meng Wang:** Writing – review & editing, Visualization, Supervision, Project administration, Investigation. **Xiaoliang Ren:** Writing – review & editing, Visualization, Project administration, Funding acquisition.

Declaration of competing interest

The authors declare no conflict of interest. All authors had read and approved the manuscript. All data were generated in-house, and no paper mill was used. All authors agree to be accountable for all aspects of work ensuring integrity and accuracy.

Acknowledgements

This work was financially supported by the National Natural Science Foundation of China (82274236) and the Tianjin Youth Technology Talent Program Grant (QN20230322).

Appendix A. Supplementary data

Supplementary data to this article can be found online at https://doi.org/10.1016/j.ijbiomac.2026.152700.

Data availability

Data will be made available on request.

References

[1] A.M. Ashour, The preventive effects of ondansetron on chemotherapy-induced nausea and vomiting in adult cancer patients: systematic review from ClinicalTrials.gov, Front. Pharmacol. 14 (2023) 1310455.
[2] S. Williamson, D. Blake, Northern Cancer Alliance Anti-Emetic Guidelines for Chemotherapy, China, 2023.
[3] A. Eghbali, F.K. Kohpar, K. Ghaffari, R.R. Afzal, A. Eghbali, A. Ghasemi, Evaluating Aprepitant single-dose plus granisetron and dexamethasone in children receiving highly emetogenic chemotherapy for the prevention of chemotherapy-induced nausea and vomiting: a triple-blinded randomized clinical trial, Cell. Ther. 45 (2023) 281–289.
[4] B. Homayun, X. Lin, H.J. Choi, Challenges and recent Progress in Oral drug delivery Systems for Biopharmaceuticals, Pharmaceutics 11 (2019) 129.
[5] N. Rommel, S. Hamdy, Oropharyngeal dysphagia: manifestations and diagnosis, Nat. Rev. Gastroenterol. Hepatol. 13 (2016) 49–59.
[6] R. Wirth, R. Dziewas, A.M. Beck, P. Clave, S. Hamdy, H.J. Heppner, S. Langmore, A.H. Leischker, R. Martino, P. Pluschinski, A. Rösler, R. Shaker, T. Warnecke, C. C. Sieber, V. Volkert, Oropharyngeal dysphagia in older persons-from pathophysiology to adequate intervention: a review and summary of an international expert meeting, Clin. Interv. Aging 11 (2016) 189–208.
[7] J. Escalante, R.M. McQuade, V. Stojanovska, K. Nurgali, Impact of chemotherapy on gastrointestinal functions and the enteric nervous system, Maturitas 105 (2017) 23–29.
[8] H. Wang, Y. Fu, J. Mao, H. Jiang, S. Du, P. Liu, J. Tao, L. Zhang, J. Zhu, Strong and tough supramolecular microneedle patches with ultrafast dissolution and rapid-onset capabilities, Adv. Mater. 34 (2022) e2207832.
[9] H. Xue, J. Jin, X. Huang, Z. Tan, Y. Zeng, G. Lu, X. Hu, K. Chen, Y. Su, X. Hu, X. Peng, L. Jiang, J. Wu, Wearable flexible ultrasound microneedle patch for cancer immunotherapy, Nat. Commun. 16 (2025) 2650.
[10] F. Damiri, N. Kommineni, S.O. Ebhodaghe, R. Bulusu, V.G.S.S. Jyothi, A.A. Sayed, A.A. Awaji, M.O. Germoush, H.S. Al-Malky, M.Z. Nasrullah, M.H. Rahman, M. M. Abdel-Daim, M. Berrada, Microneedle-based natural polysaccharide for drug delivery systems (DDS): progress and challenges, Pharmaceuticals (Basel) 15 (2022) 190.
[11] G. Ma, C. Wu, Microneedle, bio-microneedle and bio-inspired microneedle: a review, J. Control. Release 251 (2017) 11–23.
[12] X. Gao, J. Li, J. Li, M. Zhang, J. Xu, Pain-free oral delivery of biologic drugs using intestinal peristalsis-actuated microneedle robots, Sci. Adv. 10 (2024) eadj7067.
[13] B. Zheng, Q. Li, L. Fang, X. Cai, Y. Liu, Y. Duo, B. Li, Z. Wu, B. Shen, Y. Bai, S. X. Cheng, X. Zhang, Microorganism microneedle micro-engine depth drug delivery, Nat. Commun. 15 (2024) 8947.
[14] Z. Liu, X. Xu, S. Huang, X. Huang, Z. Liu, C. Yao, M. He, J. Chen, H.J. Chen, J. Liu, X. Xie, Multichannel microneedle dry electrode patches for minimally invasive transdermal recording of electrophysiological signals, Microsyst. Nanoeng. 10 (2024) 72.
[15] Y.X. Feng, H. Hu, Y.Y. Wong, X. Yao, M.L. He, Microneedles: an emerging vaccine delivery tool and a prospective solution to the challenges of SARS-CoV-2 mass vaccination, Pharmaceutics 15 (2023) 1349.
[16] J. Halder, S. Gupta, R. Kumari, G.D. Gupta, V.K. Rai, Microneedle array: applications, recent advances, and clinical pertinence in transdermal drug delivery, J. Pharm. Innov. 16 (2021) 558–565.
[17] J.H. Tay, Y.H. Lim, M. Zheng, Y. Zhao, W.S. Tan, C. Xu, U. Ramamurty, J. Song, Development of hyaluronic acid-silica composites via in situ precipitation for improved penetration efficiency in fast-dissolving microneedle systems, Acta Biomater. 172 (2023) 175–187.
[18] B. Cai, Y. Gong, Z. Wang, L. Wang, W. Chen, Microneedle arrays integrated with living organisms for smart biomedical applications, Theranostics 11 (2021) 10012–10029.
[19] Y. Tian, L. Lu, Recent advances in self-assembling peptide matrices as functional coatings for implantable devices, Front. Chem. 10 (2022) 1040499.
[20] M. Saif, M.A. Raza, V.B. Patravale, Polysaccharide copolymeric conjugates and their applications in targeted cancer therapy, Int. J. Biol. Macromol. 327 (2025) 147380.
[21] Z. Zhu, T. Liang, G. Dai, J. Zheng, J. Dong, C. Xia, B. Duan, Extraction, structural-activity relationships, bioactivities, and application prospects of Bletilla striata polysaccharides as ingredients for functional products: a review, Int. J. Biol. Macromol. 245 (2023) 125407.
[22] L. Zhang, X. Shi, X. Zhang, T. Chen, S. Liao, J. Gao, Z. Zhou, M. Zhang, F. Peng, A comprehensive review of ethnopharmacology, phytochemistry, pharmacological effects, and quality control of Bletilla striata, J. Ethnopharmacol. 353 (2025) 120273.
[23] Y. Liu, C. Sun, G. Zhang, J. Wu, L. Huang, J. Qiao, Q. Guan, Bio-responsive Bletilla striata polysaccharide-based micelles for enhancing intracellular docetaxel delivery, Int. J. Biol. Macromol. 142 (2020) 277–287.
[24] K. Gou, Y. Li, Y. Qu, H. Li, R. Zeng, Advances and prospects of Bletilla striata polysaccharide as promising multifunctional biomedical materials, Mater. Des. 223 (2022) 111198.

[25] C. Fu, X. Deng, J. Gao, Characterization of the polysaccharide from *Bletilla striata* and its inhibitory effects on amylolytic enzymes and prebiotic activity, Front. Nutr. 12 (2025) 1625260.
[26] D. Sun, M. Wang, D. Ji, J. Qiao, T. He, X. Lin, Q. Guan, Synthesis of a reduction-sensitive *Bletilla striata* polysaccharide amphiphilic copolymer, Chin. Chem. Lett. 29 (2018) 831–833.
[27] S. Jakfar, T.C. Lin, Z.Y. Chen, I.H. Yang, B.A. Gani, D.S. Ningsih, H. Kusuma, C. T. Chang, F.H. Lin, A polysaccharide isolated from the herb *Bletilla striata* combined with methylcellulose to form a hydrogel via self-assembly as a wound dressing, Int. J. Mol. Sci. 23 (2022) 12019.
[28] N. Zhang, L. Xue, A. Younas, F. Liu, J. Sun, Z. Dong, Y. Zhao, Co-delivery of triamcinolone acetonide and verapamil for synergistic treatment of hypertrophic scars via carboxymethyl chitosan and *Bletilla striata* polysaccharide-based microneedles, Carbohydr. Polym. 284 (2022) 119219.
[29] Y. Zhao, Q. Wang, S. Yan, J. Zhou, L. Huang, H. Zhu, F. Ye, Y. Zhang, L. Chen, L. Chen, T. Zheng, *Bletilla striata* polysaccharide promotes diabetic wound healing through inhibition of the NLRP3 Inflammasome, Front. Pharmacol. 12 (2021) 659215.
[30] C. Zhao, L. Huang, J. Tang, L. Lv, X. Wang, X. Dong, F. Yang, Q. Guan, Multifunctional nanofibrous scaffolds for enhancing full-thickness wound healing loaded with Bletilla striata polysaccharides, Int. J. Biol. Macromol. 278 (Pt 1) (2024) 134597.
[31] L. Yang, X. Wang, A. Hou, J. Zhang, S. Wang, W. Man, H. Yu, S. Zheng, Q. Wang, H. Jiang, H. Kuang, A review of the botany, traditional uses, phytochemistry, and pharmacology of the Flos Inulae, J. Ethnopharmacol. 276 (2021) 114125.
[32] J. Zhang, M. Zhang, W.H. Zhang, Q.M. Zhu, X.K. Huo, C.P. Sun, X.C. Ma, H.T. Xiao, Total flavonoids of Inula japonica alleviated the inflammatory response and oxidative stress in LPS-induced acute lung injury via inhibiting the sEH activity: insights from lipid metabolomics, Phytomedicine 107 (2022) 154380.
[33] J.H. Choi, Y.N. Park, Y. Li, M.H. Jin, J. Lee, Y. Lee, J.K. Son, H.W. Chang, E. Lee, Flowers of Inula japonica attenuate inflammatory responses, Immune Netw. 10 (5) (2010) 145–152.
[34] K. Kinoshita, T. Kawai, T. Imaizumi, Y. Akita, K. Koyama, K. Takahashi, Anti-emetic principles of Inula linariaefolia flowers and Forsythia suspensa fruits, Phytomedicine 3 (1) (1996) 51–58.
[35] X. Sun, F. Nie, J. Sun, J. Zhang, Y. Wang, Medicinal plants for chemotherapy-induced nausea and vomiting: a systematic review of antiemetic, Chemosensitizing, and immunomodulatory mechanisms, Ther. Clin. Risk Manag. 21 (2025) 1187–1218.
[36] J. Mikuła-Pietrasik, A. Witucka, M. Pakuła, P. Uruski, B. Begier-Krasińska, A. Niklas, A. Tykarski, K. Książek, Comprehensive review on how platinum- and taxane-based chemotherapy of ovarian cancer affects biology of normal cells, Cell. Mol. Life Sci. 76 (2019) 681–697.
[37] S.S. Li, Y.J. Hou, L. Zhang, Y. Dong, S.H. Liu, B. Li, C.C. Zhang, X.N. Yang, R.L. You, H.Y. Xu, B. Li, Historical evolution of Xuanfu Daizhe decoction, Zhongguo. Zhong. Yao. Za. Zhi. 47 (2022) 4033–4041.
[38] Z.R. Yang, H. Suo, J.W. Fan, N. Lv, K. Du, T. Ma, H. Qin, Y. Li, L. Yang, N.Y. Zhou, H. Jiang, J. Tao, J. Zhu, Endogenous stimuli-responsive separating microneedles to inhibit hypertrophic scar through remodeling the pathological microenvironment, Nat. Commun. 15 (2024) 2038.
[39] S.R. Son, K.S. Kim, D.S. Jang, S. Lee, Caffeoylglucaric and Caffeoylquinic acids from *Inula japonica* leaves and their anti-skin aging effects in TNF-α-induced Normal human fibroblast damage, J. Agric. Food Chem. 73 (22) (2025) 13471–13487.
[40] J. Li, X. Guo, Z. Luo, D. Wu, X. Shi, L. Xu, Q. Zhang, C. Xie, C. Yang, Chemical constituents from the flowers of Inula japonica and their anti-inflammatory activity, J. Ethnopharmacol. 318 (2024) 117052.
[41] J. Li, L. Niu, H. Huang, Q. Li, C. Yang, C. Xie, 1-O-Acetylbritannilactone exerts anti-inflammatory and anti-MUC5AC effects by targeting PKC-α and downregulating the SRC/EGFR/MAPK signaling pathway, Int. Immunopharmacol. 161 (2025) 114979.
[42] A. Younas, Z. Dong, Z. Hou, M. Asad, M. Li, N. Zhang, A chitosan/fucoidan nanoparticle-loaded pullulan microneedle patch for differential drug release to promote wound healing, Carbohydr. Polym. 306 (2023) 120593.
[43] Y. Cui, Y. Mo, Q. Zhang, W. Tian, Y. Xue, J. Bai, S. Du, Microneedle-assisted percutaneous delivery of Paeoniflorin-loaded Ethosomes, Molecules 23 (2018) 3371.
[44] M.I. Love, W. Huber, S. Anders, Moderated estimation of fold change and dispersion for RNA-seq data with DESeq2, Genome Biol. 15 (2014) 550.
[45] G. Yu, L.G. Wang, Y. Han, Q.Y. He, ClusterProfiler: an R package for comparing biological themes among gene clusters, OMICS 16 (2012) 284–287.
[46] M. Ying, J. Feng, M. Liu, L. Wang, J. Liu, TCMNP: a data processing and visualization database and R package for traditional Chinese medicine network pharmacology, Pharmacol. Res. Mod. Chin. Med. 14 (2025) 100562.
[47] Y. Zhang, Z. Chen, W. Wu, C. Xu, Focused ion beam (FIB) prepared microtextured microneedle array capable of delivering drugs through punctured skin, Sci. Rep. 14 (1) (2024) 31489.
[48] Z. Faraji Rad, P.D. Prewett, G.J. Davies, High-resolution two-photon polymerization: the most versatile technique for the fabrication of microneedle arrays, Microsyst. Nanoeng. 7 (2021) 71.
[49] P. Makvandi, M. Kirkby, A.R.J. Hutton, M. Shabani, C.K.Y. Yiu, Z. Baghbantaraghdari, R. Jamaledin, M. Carlotti, B. Mazzolai, V. Mattoli, R. F. Donnelly, Engineering microneedle patches for improved penetration: analysis, skin models and factors affecting needle insertion, Nano Micro Lett. 13 (2021) 1–41.
[50] P. Zhou, S. Zhao, C. Huang, Y. Qu, C. Zhang, *Bletilla striata polysaccharide microneedle for effective transdermal administration of model protein antigen*, Int. J. Biol. Macromol. 205 (2022) 511–519.
[51] J.Z. Liu, L. Wang, L.J. Jiang, H.C. Lyu, Q. Yuan, G.F. Wang, Y.J. Fu, Q. Cui, In sight the behavior of natural *Bletilla striata* polysaccharide hydrocolloids by molecular dynamics method, Int. J. Biol. Macromol. 266 (Pt 1) (2024) 131245.
[52] Z. Hu, K. Zhao, X. Rao, X. Chen, Y. Niu, Q. Zhang, M. Zhou, Y. Chen, F. Zhou, J. Yu, Z. Ding, B. Zhu, Microenvironment-responsive *Bletilla* polysaccharide hydrogel with photothermal antibacterial and macrophage polarization-regulating properties for diabetic wound healing, Int. J. Biol. Macromol. 283 (Pt 4) (2024) 137819.
[53] K. Biniek, J. Kaczvinsky, P. Matts, R.H. Dauskardt, Understanding age-induced alterations to the biomechanical barrier function of human stratum corneum, J. Dermatol. Sci. 80 (2) (2015) 94–101.
[54] K.P. Azarikhah, M. Saifullah, Z. Faraji Rad, Age-dependent finite element analysis of microneedle penetration into human skin: influence of insertion velocity, and microneedle's geometry and material, Macromol. Mater. Eng. 310 (2025) e00123.
[55] Q.K. Anjani, A.D.C. Nainggolan, H. Li, A. Miatmoko, E. Larrañeta, R.F. Donnelly, Parafilm® M and Strat-M® as skin simulants in in vitro permeation of dissolving microarray patches loaded with proteins, Int. J. Pharm. 655 (2024) 124071.
[56] D. Chen, Y. Guo, Y. Yang, Liujunanwei decoction attenuates cisplatin-induced nausea and vomiting in a rat-Pica model partially mediated by modulating the gut micsrobiome, Front. Cell. Infect. Microbiol. 12 (2022) 876781.
[57] S. Li, Y. Lei, J.D.Z. Chen, Chemotherapy-induced Pica in rats reduced by Electroacupuncture, Neuromodulation 21 (3) (2018) 254–260.
[58] K. Yamamoto, K. Asano, A. Tasaka, Y. Ogura, S. Kim, Y. Ito, A. Yamatodani, Involvement of substance P in the development of cisplatin-induced acute and delayed pica in rats, Br. J. Pharmacol. 171 (11) (2014) 2888–2899.
[59] M. Abe, T. Yamaguchi, Y. Fujita, T. Nishimura, K. Kitagawa, N. Inui, K. Hirano, Y. Sakata, H. Iihara, Y. Shibuya, K. Suzuki, K. Shibata, K. Hori, H. Daga, T. Nakayama, Y. Sakata, T.Y. Takahashi, S. Zenda, H. Hashimoto, Efficacy of olanzapine in addition to standard triplet antiemetic therapy for cisplatin-based chemotherapy: a secondary analysis of the J-FORCE randomized clinical trial, JAMA Netw. Open 6 (5) (2023) e2310894.
[60] C.C. Chu, C.H. Hsing, J.P. Shieh, C.C. Chien, C.M. Ho, J.J. Wang, The cellular mechanisms of the antiemetic action of dexamethasone and related glucocorticoids against vomiting, Eur. J. Pharmacol. 722 (2014) 48–54.
[61] X. He, L. Liu, F. Gu, R. Huang, L. Liu, Y. Nian, Y. Zhang, C. Song, Exploration of the anti-inflammatory, analgesic, and wound healing activities of *Bletilla striata* polysaccharide, Int. J. Biol. Macromol. 261 (Pt 2) (2024) 129874.
[62] L. Bai, T. Wang, Q. Deng, W. Zheng, X. Li, H. Yang, R. Tong, D. Yu, J. Shi, J, Dual properties of pharmacological activities and preparation excipient: *Bletilla striata* polysaccharides, Int J biol Macromol.International 254 (Pt 1) (2024) 127643.
[63] S. Agre, M. Agre, P. Pol, M. Tonse, M. Mohanty, A. Shaikh, Retrospective evaluation of a dexamethasone sparing antiemetic regimen: an antiemetic prophylaxis study on NEPA (Netupitant plus Palonosetron) for preventing chemotherapy-induced nausea and vomiting (CINV) in Cancer patients, Cureus 15 (2023) e49763.
[64] Z. Guo, P. Chen, L. Liu, H. Song, Compatibility and stability of methylprednisolone sodium succinate and granisetron hydrochloride in 0.9% sodium chloride solution, Medicine (Baltimore) 101 (2022) e29674.
[65] L. Sun, L. Jin, C. Jiao, L. Wang, Q. Xu, H. Wu, X. Chen, Comparison of the ED50 of prophylactic butorphanol in preventing morphine-induced pruritus with or without palonosetron: a prospective, double-blinded, randomized dose-response trial using an up-down sequential allocation method, Ann. Med. 55 (2023) 2304671.
[66] A. Linan-Rico, F. Ochoa-Cortes, A. Beyder, S. Soghomonyan, A. Zuleta-Alarcon, V. Coppola, F.L. Christofi, Mechanosensory signaling in Enterochromaffin cells and 5-HT release: potential implications for gut inflammation, Front. Neurosci. 10 (2016) 564.